

z' -band ground-based detection of the secondary eclipse of WASP-19b

J. R. Burton¹, C. A. Watson¹, S. P. Littlefair², V. S. Dhillon²,
N. P. Gibson³, T. R. Marsh⁴, D. Pollacco¹

jburton04@qub.ac.uk

ABSTRACT

We present the ground-based detection of the secondary eclipse of the transiting exoplanet WASP-19b. The observations were made in the Sloan z' -band using the ULTRACAM triple-beam CCD camera mounted on the NTT. The measurement shows a $0.088 \pm 0.019\%$ eclipse depth, matching previous predictions based on H - and K -band measurements. We discuss in detail our approach to the removal of errors arising due to systematics in the data set, in addition to fitting a model transit to our data. This fit returns an eclipse centre, T_0 , of 2455578.7676 HJD, consistent with a circular orbit. Our measurement of the secondary eclipse depth is also compared to model atmospheres of WASP-19b, and is found to be consistent with previous measurements at longer wavelengths for the model atmospheres we investigated.

Subject headings: planets and satellites: atmospheres – planets and satellites: individual (WASP-19b) – stars: solar-type

1. Introduction

Transiting exoplanetary systems provide an excellent opportunity to measure the physical properties of exoplanets, and can allow for the atmospheric composition and structure to be investigated. The primary transit (where the planet occults the star), combined with radial velocity measurements mean key planetary parameters, such as the radius and mass,

¹Astrophysics Research Centre, Queen’s University Belfast, Belfast, BT7 1NN, UK

²Department of Physics and Astronomy, University of Sheffield, Sheffield, S3 7RH, UK

³Department of Physics, University of Oxford, Oxford, OX1 3RH, UK

⁴Department of Physics and Astronomy, University of Warwick, Coventry, CV4 7AL, UK

can be inferred for the exoplanetary system. The secondary eclipse, where the planet passes behind the sky-projected disc of the star, allows for the direct detection of flux from the exoplanet, meaning properties of the planet can be directly measured, instead of derived from the transit light curve or the radial velocity. For example, observations of the secondary eclipse provides information on the temperature (Knutson et al. 2007) and atmospheric constituents (e.g. Burrows et al. 2005, Burrows et al. 2006) of the exoplanet, and has been a powerful tool into the study of hot-Jupiters and their atmospheres. Previous work on secondary eclipses has mostly been carried out from space-based platforms (notably the Spitzer space telescope, e.g. Laughlin et al. 2009, Deming et al. 2010), but recent work has been focused on obtaining secondary eclipse detections from the ground (e.g. de Mooj & Snellen 2009, Alonso et al. 2010, Zhao et al. 2011).

The transiting exoplanet WASP-19b (Hebb et al. 2010) has one of the shortest-known orbital periods of 0.79 days. The level of irradiation incident on the planetary surface, coupled with poor heat redistribution (Fortney et al. 2008) makes WASP-19b one of the hottest known transiting exoplanets. In addition to this, systems with short periods such as these are subject to intense tidal forces (e.g. Leconte et al. 2011), meaning WASP-19b is an extremely interesting case for both atmospheric composition and structure models. The secondary transit of WASP-19b has previously been observed from the ground in the H - and K -bands using the HAWK-I (High Acuity Wide-field K-band Imager) instrument mounted on the VLT (Anderson et al. 2010, Gibson et al. 2010). The secondary eclipse depth in these studies was found to be $0.259 \pm 0.045\%$ and $0.366 \pm 0.072\%$ respectively, corresponding to a dayside brightness temperature of $\sim 2500\text{K}$ in both cases. From this, the authors concluded that there was poor heat redistribution from dayside to nightside, and demonstrated from the phase offset of the eclipse centre that the orbit of WASP-19b is consistent with a circular orbit.

In this paper, we present a ground-based secondary eclipse observation of WASP-19b in the Sloan z' -band (centred on 909.7nm). We discuss the data acquisition and reduction, along with the limitations associated with our ground-based observations, and potential follow-up work. This is only the 3rd z' -band detection of an exoplanet secondary eclipse from the ground, the first being OGLE-TR-56b (Sing & López-Morales 2009), and the second being WASP-12b (López-Morales et al. 2010).

2. Observations

On the 17th January 2011, the $m_v=12.3$ star WASP-19 was observed from UT 01:56-09:02. It was observed simultaneously in the Sloan- u' , g' and z' bands using the high

speed CCD camera ULTRACAM (see Dhillon et al. 2007 for a description) on the European Southern Observatory (ESO) 3.5m New Technology Telescope (NTT) based at La Silla, Chile. The frame-transfer capability of ULTRACAM means that there is negligible deadtime (~ 25 ms) between exposures, maximising the efficiency of observations. This high-efficiency mode allows for the chip to be read out while the next data frame is being exposed, meaning the CCD can obtain thousands of images per night, in addition to exposing in three bands at once.

In order to maximise the precision during the observations, we opted to defocus the telescope (see e.g. Southworth et al. 2009 for an in-depth description of the rationale and techniques). This was further assisted thanks to ULTRACAM’s design allowing for approximately 600 twilight flat-field-frames to be taken per night, giving an excellent characterisation of the pixel-to-pixel variations of the CCD. A number of steps were also taken to ensure the observations were as free from systematics as possible whilst at the telescope. A previous observing run using ULTRACAM on the NTT had discovered variable vignetting over the edge of the chip as a result of the positioning of the guide probe. In order to ensure this did not happen during our exposures, the guide probe position was carefully selected such that vignetting was avoided throughout the observations, and positioned out of the beam when obtaining flat fields.

While acquiring flat-field exposures, the telescope was spiralled so that any stars present did not remain on the same pixel over consecutive images. Sky flats were also taken near the zenith where the sky brightness as a function of altitude varies the least, minimising gradients across the chip. Over the course of the data collection, utmost care was taken for the target to remain on the same position on the chip. We carefully picked the guide star to avoid vignetting by the guide probe, continuously monitored both the x- and y-position of the target on the ULTRACAM CCD in real time, and manually corrected any drift when necessary. Doing this allowed for the drift of the target to be less than one pixel throughout the majority of the night (the mean motion of the target over all the frames was calculated to be 0.47 pixels or $0.16''$). The telescope was defocussed so that the objects’ point spread function (PSF) had a full-width at half-maximum (FWHM) of $4\text{--}5''$. Since the WASP-19 field has a number of objects at a relatively small separation from the target, $4\text{--}5''$ defocus was found to be the maximum possible before blending with background objects might have become an issue. Observation conditions over the night were very good, with seeing remaining at $\sim 1''$ over the course of the exposures. In addition to this, we also used the simultaneously-recorded g' -band to monitor the surface activity of the star, again, in real time. Doing this also allowed us to analyse the z' -band light curve for systematics (since the secondary eclipse signal of the planet is too faint to see in the g' -band), and since the spot/photosphere contrast is higher in the g' -band compared to the z' -band, any features on

timescales longer than the secondary eclipse could also be monitored with a high degree of precision.

3. Calibration

4524 data frames were obtained per filter over the course of the night, each with an exposure time of ~ 5.7 s. We obtained approximately 120 minutes of pre-ingress data, and 90 minutes of post-egress data, meaning the out-of-eclipse portion of the lightcurve would be well-characterised (the predicted secondary eclipse duration for WASP-19b is 92.4 minutes as a comparison). Once the data had been obtained, photometry was performed first by de-biasing and applying flat-fields in the usual way. The ULTRACAM pipeline¹ was used to create apertures around the target and six bright comparison objects in the field of view (see figure 1). The apertures were set to a fixed radius, and the source position was tracked using a moffat fit on each frame. We also ran the entire data extraction using a Gaussian fit in order to ensure that different tracking methods did not affect how the sources were tracked over the course of observations, and there was no difference in the resulting lightcurves. The object aperture was set to a radius of 18 pixels. The inner sky aperture, used for sampling the background level, was set to a radius of 26 pixels and the outer sky aperture was set to a radius of 100 (we note here that a number of different aperture sizes were trialled, and as long as a reasonable sky background was sampled, this did not affect the target or comparison lightcurves). Since a number of background objects were in this aperture, these were masked out in order to remove them from the sky background estimation. Differential photometry was then performed on the target by dividing by the average flux of the six reference stars in the field. For the g' -band, only 5 comparisons were used since one of the reference stars became too heavily blended with 2 background objects. The u' -band had only 2 visible comparison objects, as the majority of the stars were too faint to be detected at this shorter wavelength. We do not present any of the u' -band data due to the lack of suitable comparison objects and hence, the noise present in the lightcurve.

4. Data Analysis

Given the challenges of obtaining a ~ 1 mmag secondary eclipse detection, the majority of our data analysis has been concentrated on characterising and removing systematics that arise as a result of our ground-based observations as well as identifying any correlations

¹<http://deneb.astro.warwick.ac.uk/phsaap/ultracam>

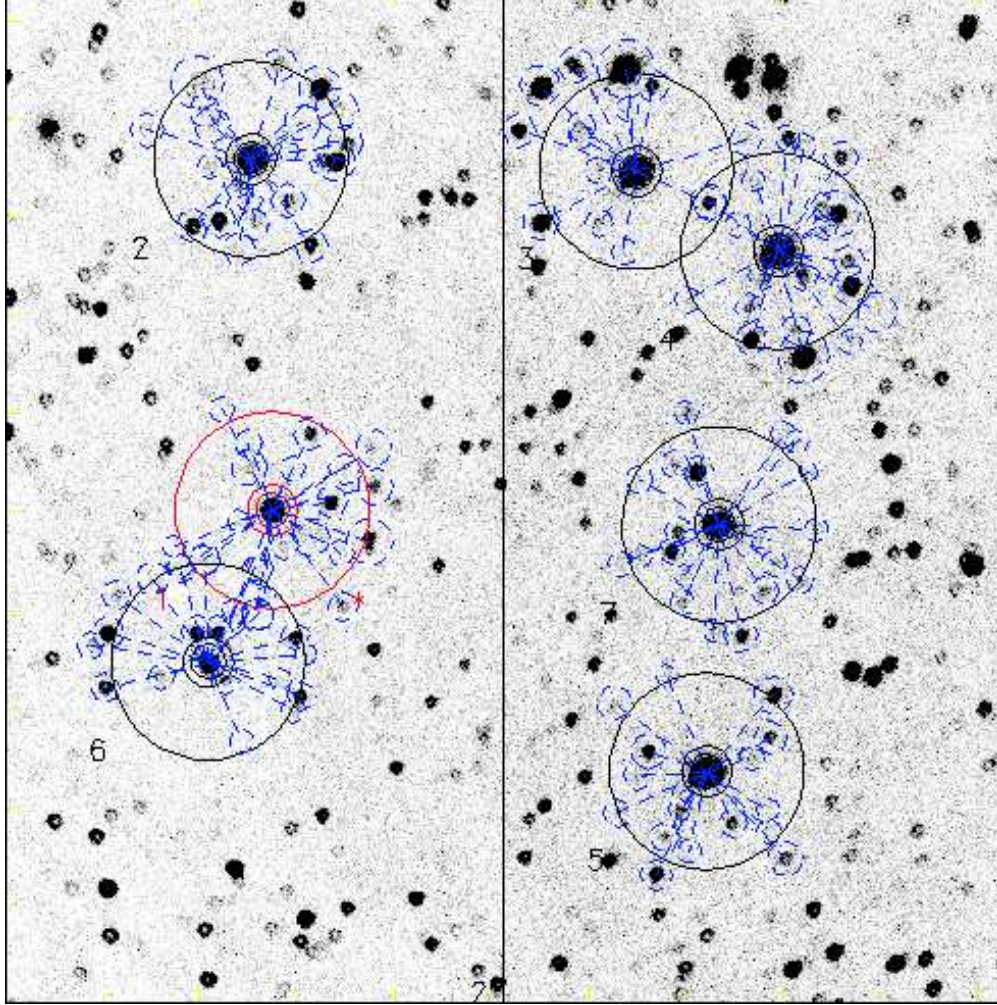


Fig. 1.— z' -band data frame showing the WASP-19 field, after the colours have been inverted for the sake of clarity. North is directed upwards and east is to the left in this image. The target is located in the red (light grey) aperture (left-hand panel, middle object), and the six comparisons used are shown in the remaining apertures. These indicate the sky and target apertures used for the z' -band data reduction. The smaller dashed apertures (blue/dark grey) indicate objects which have been masked out from the sky background. The field-of view (FOV) in our case measures 6 arcminutes.

which appear to be present. This section focuses on our method of identifying and removing systematic errors using a ‘weighting’ method in the comparison lightcurve, along with the process of decorrelation to ensure the target lightcurve is as free from systematics as possible. We also describe the fitting of a model transit to the data to infer the secondary eclipse depth and error.

4.1. Systematics

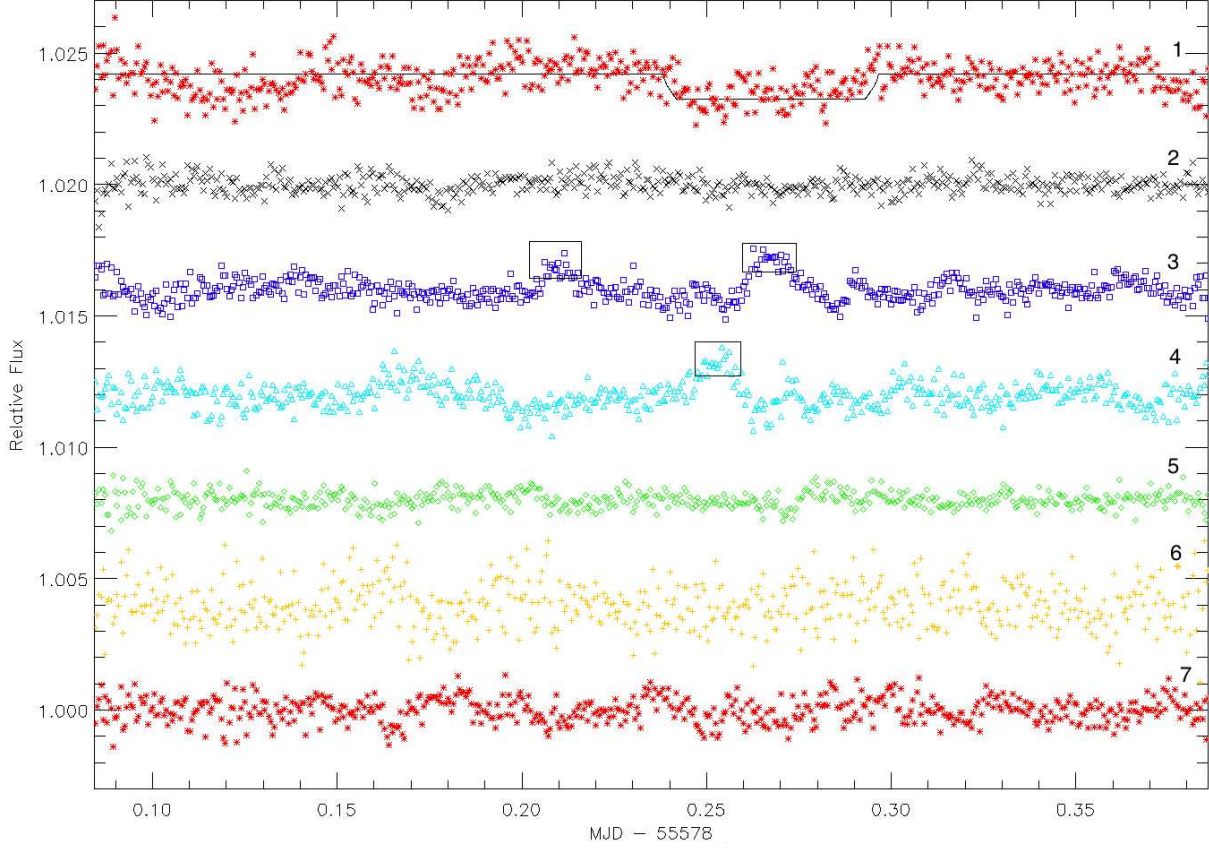


Fig. 2.— Normalised lightcurves (using a 2nd-order polynomial fit) of the target (1) and the six comparisons (2-7) corresponding to the objects shown in figure 1 after dividing through by the total comparison lightcurve. The model transit (black line) is our initial Mandel-Agol fit (see section 4.3). The 3 boxed sections in comparisons 3 and 4 indicates regions where systematic ‘spikes’ flagged by our analysis (see text) were high. We note here that these data points have not been rejected outright, but are merely indications of regions in which our systematic analysis flagged a number of systematic errors. At these times, these comparisons are rejected and the remaining weighting factors are adjusted to remove this effect from the total lightcurve.

Since our observations were made from the ground, systematics may be appreciable compared to the signal from any potential secondary eclipse detections. As is normal when carrying out differential photometry, we obtained the final WASP-19 lightcurve, $L(t)$, at time t using the following formula:

$$L(t) = \frac{T(t)}{a_1(t)C_1(t) + a_2(t)C_2(t) + \dots + a_n(t)C_n(t)}, \quad (1)$$

where $T(t)$ is the raw flux from the target, $C_n(t)$ is the flux from comparison star ‘n’, and $a_n(t)$ is the weighting factor of comparison ‘n’. When carrying out differential photometry, the weighting factor is normally set to 1. In our analysis, however, we allow for the weighting factor to be switched to 0 depending on whether we identify a systematic in the raw lightcurve of the comparison object. The other weighting factors for the remaining comparisons are then adjusted together to take into account the missing flux due to the rejected comparison contribution. In our analysis, if the contribution from the comparison showed a sustained run of points which lay more than 1σ from a local mean, we rejected these points as due to a systematic – essentially if the $a_n(t)$ value in equation (1) was abnormally high or low for a number of consecutive data points. We defined a systematic region as any run of 6 or more consecutive points, all of which lay $>1\sigma$ above or below the mean contribution for that comparison. Statistically, the chances of this happening are $<0.001\%$. Once this analysis had been carried out for all comparisons, the points which had been rejected due to systematics were flagged in the total comparison lightcurve, and the weighting factors of the remaining comparisons adjusted such that this systematic was removed. Extreme care was taken to only adjust for points which showed systematic errors so as not to falsely idealise the comparison lightcurve. Figure 2 shows the lightcurves of WASP-19 (1), along with each of the comparisons (2-7), corresponding to the numbered annuli in figure 1. The boxed sections indicate regions which contained a high concentration of points which were flagged as systematics in our analysis. The majority of points rejected appear to be in comparison objects 3 and 4. As can be seen from figure 1, these objects have a large number of background objects, some of which are of appreciable brightness, and appear near the edge of the right-hand side of the CCD. This may go some way as to explaining why these objects show an increase in systematics at these times, as some background stars may have leaked into the sky annulus over these observations. In addition to this, some level of vignetting may remain, these two objects being the most susceptible to being affected due to their close proximity to the upper edge of the CCD and their close proximity to each other. The rejected points can then be removed, the contributions of the remaining comparisons increased, and the lightcurve of the target improved. Upon comparison of the pre- and post-correction lightcurves of WASP-19, little difference is noticeable in a significant number of data points once we remove any points flagged as a systematic. Even when reducing the number of consecutive $1\text{-}\sigma$ outliers to 5 or even 4, the difference is minimal. This indicates that the WASP-19 lightcurve is robust against the systematics that we have identified arising in the comparison lightcurves. This is probably due to the fact that we have enough good comparison objects in the field to remove any significant systematic errors before our analysis.

4.2. Correlations

The presence of a correlation or anti-correlation between the flux from the target and another parameter (such as position of the star on the chip, airmass, sky background etc.) may indicate that any features present in the lightcurve (e.g. a systematic mimicking a secondary eclipse) could be related to this correlation. During our data analysis, all parameters which we were able to quantify were thoroughly tested for the presence of correlations, and if there was evidence of this, a decorrelation could be applied to check if the secondary eclipse feature remained. We thoroughly tested the following for correlations against the flux from the target; x-position, y-position, mean position (i.e. simultaneous x- and y-position on the CCD), sky background, airmass (altitude), azimuth and seeing (the FWHM of the target’s PSF), in addition to investigating the relationship between the wavelength bands themselves (i.e. a direct comparison between the z' -band and g' -band). The resulting plots (see appendix) indicate that the strongest correlation was between the z' -band and sky background, where there appears to be almost a 2-component trend, where the lower sky counts appear to correlate with higher z' -band fluxes. This is shown in figure 3, in which the points where the planet is predicted to be in secondary eclipse are highlighted. All of the other parameters which we tested for showed either no significant correlations or showed low-level correlation which disappeared after the sky correction. This analysis was also applied to each of the comparison objects in turn, in order to check for the same correlations.

Plotting the lightcurve of the sky as a function of time reveals a number of features present in the sky background over the course of observations. Figure 4 shows a number of features pre-ingress (i.e. before 0.21MJD) and post egress - when we entered dawn twilight. It can also be seen that there are no major features present in the sky background during the predicted secondary eclipse (~ 0.23 -0.3MJD), other than a general slope. This indicates that the sky background was well-behaved and free of any major features which may impact the target lightcurve during secondary eclipse. We note here that all correlations and tests for systematics have been cut off before 0.35MJD due to the sharp increase in sky background (due to the sunrise) after this time. It is also important to state that the object transited across the meridian just after egress (0.3MJD).

In order to adjust for the sky background, we first modelled the correlation using a polynomial fit. We then found the average value of the z' -band flux, and used this in our polynomial formula to give an adjustment factor for each data point. We then simply divided our target lightcurve by this adjustment factor in order to remove the correlation with sky. In addition to the polynomial fit, a number of other methods were also used to model the correlation (e.g. spline fit, linear fit). However, an important factor was to be able to smoothly vary from one component into the other, something which was fairly difficult to

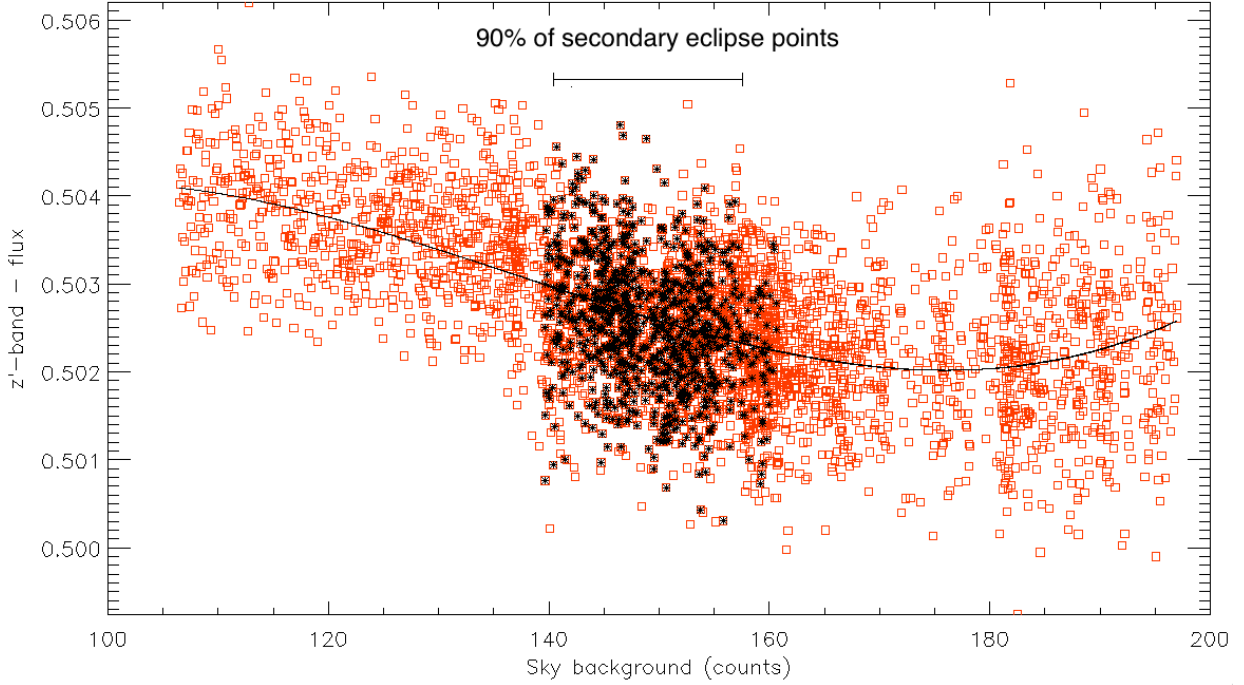


Fig. 3.— Sky vs. target z' -band, along with the 3rd-order polynomial we used to fit the trend. Points where the planet is predicted to be in secondary eclipse have been highlighted in black (asterisks). The horizontal bar indicates the range in sky background counts over which 90% of the secondary eclipse points lie.

satisfactorily achieve using a spline fit. We opted to use a 3rd-order polynomial fit based on this, combined with the fact that the polynomial did remove the effects of sky brightness to an excellent degree. We tested higher-order polynomials (4th and 5th term), but the fit provided by these resulted in an over-correction, due to the spread of the points in figure 4. With higher order fits, we also found that the points in the lightcurve where the planet is in egress were affected, as these points lay where the sky brightness correlation changed rapidly. This meant we were extremely cautious both when applying our correlation correction to the target lightcurve as well as fitting the model to the secondary eclipse. We also tested how changing the polynomial at the lower sky brightness affected the target lightcurve. We discovered that altering the polynomial below 140 counts altered the post-egress data points, noting that the secondary eclipse feature was not affected by altering the order of the polynomial. This can be seen in figure 3, where the points which correspond to the secondary eclipse (black points) are all located in the main concentration of data points (i.e. 140-170 counts sky background). The result of this correction is shown in figure 5, below.

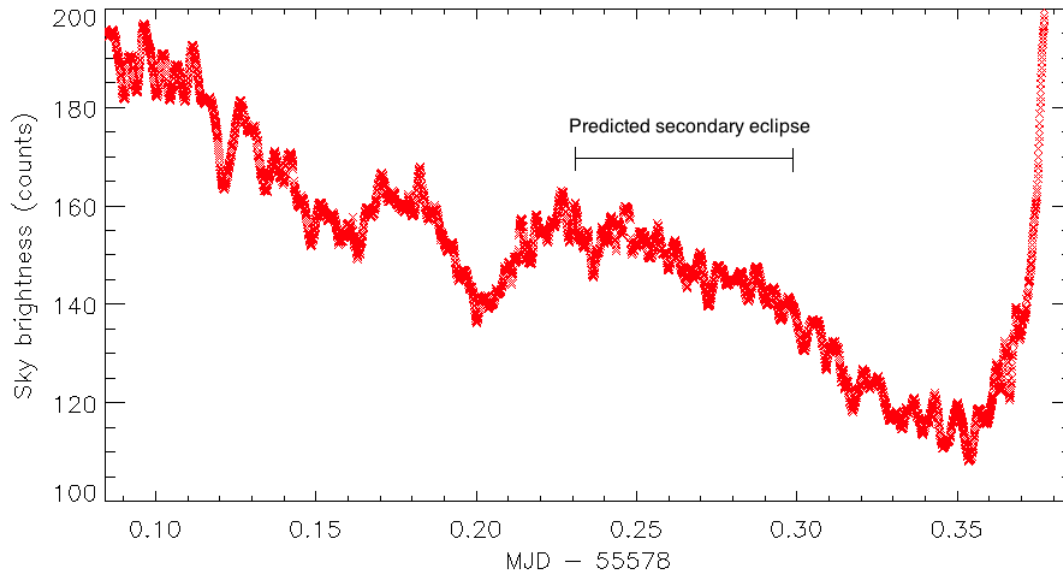


Fig. 4.— z' -band sky background over the course of observing. Note the numerous features in the lightcurve, especially the points between 0.15-0.22 MJD (i.e. just before the planet enters secondary eclipse). Altering these points had a direct effect on the target lightcurve, indicating the care which must be taken when dealing with the sky background.

4.3. Transit fitting

In order to fit the lightcurve, a simple model transit was generated using the technique outlined by Mandel & Agol (2002) of an opaque disc occulting a second disc. For this, we assumed zero limb darkening for the exoplanet. Once the systematic and decorrelation analysis had been carried out, the best fit to this secondary eclipse using the Markov-Chain-Monte-Carlo (MCMC) technique was found, the approach of which is described by Collier-Cameron et al. (2007). Initially, we made the assumption that the planet is in a circular orbit around the star, and in addition the secondary eclipse times for the night we observed were fixed and accurate (in the second step of our fitting process, we allowed the transit duration, and the eclipse centre time – T_0 – to vary). In order to obtain the correct depth and associated error, we used the Transit Analysis Package (TAP)² to model our single transit. This is a GUI written for IDL which allows for MCMC analysis to be performed with a number of user-defined system parameters (mass ratio, period, eclipse centre, eccentricity and inclination of the system). Since we were assuming the feature present in

²<http://ifa.hawaii.edu/users/zgazak/IfA/TAP.html>

the lightcurve was the actual secondary eclipse, the system parameters were fixed based on the values given by Hellier et al. (2011). Our priority in this analysis was solely to obtain the eclipse depth and errors (termed ‘white noise’ in the TAP interface), which meant fixing the system parameters was justified (in the same manner as Gibson et al. 2010). The TAP returned an eclipse depth and associated error of $0.1\pm0.02\%$ (1.0 ± 0.2 mmag). We then double-checked the results from the TAP using the secondary eclipse fitting routines of Gibson et al. (2010). Since these have had a legacy of successful secondary eclipse fitting (for the same planetary system), these routines were the preferred choice to fit the eclipse depth, transit times and error. Upon employing the Gibson routines, the system parameters used were, again, from Hellier et al. (2011), and fixed in the MCMC run. After running the routines of Gibson et al. (2010) several times whilst fixing the transit duration, the eclipse depth was found to be $0.081\pm0.018\%$ (0.81 ± 0.18 mmag), in close agreement with the result from the TAP. In the case where we allowed the transit duration to vary, however, we returned an eclipse depth of $0.088\pm0.019\%$ (0.88 ± 0.19 mmag). This was due to a shorter transit time allowing for fewer points to lie above the model, resulting in a better fit of the model to the data. When we isolate the secondary eclipse by opting to fit the transit between 0.22 and 0.32MJD from the same initial model, we return the same eclipse depth with a slightly reduced error - $0.088\pm0.015\%$. This is due to the fact that we are analysing fewer points which lie predominantly above the normalisation level just before and after the secondary eclipse feature. Out of the two eclipse depths we return, we have opted to draw our conclusions from the analysis where we allowed the transit duration to vary, since our single night’s data cannot put constraints on the transit duration and T_0 value with too high a level of confidence. We have also opted to draw our conclusions from the total lightcurve duration fit, as this gives a better indication of the errors present in the out-of-eclipse baseline. Table 1 shows the parameters which resulted from the MCMC analysis, and the final secondary eclipse is shown in figure 5.

| Table 1: MCMC parameters | | | |
|--------------------------|--------|-------------------------|------|
| Parameter | Symbol | MCMC values | Unit |
| Eclipse depth | D | 0.088 ± 0.019 | % |
| Transit centre | T_0 | 2455578.7676 ± 0.0039 | HJD |

Parameters from our final MCMC fitting routine.

5. Results

The target lightcurve is shown in figure 5. As can be seen from the uncorrected lightcurve (central data points), at time 0.1 to 0.14MJD, there appears to be a feature of a similar depth

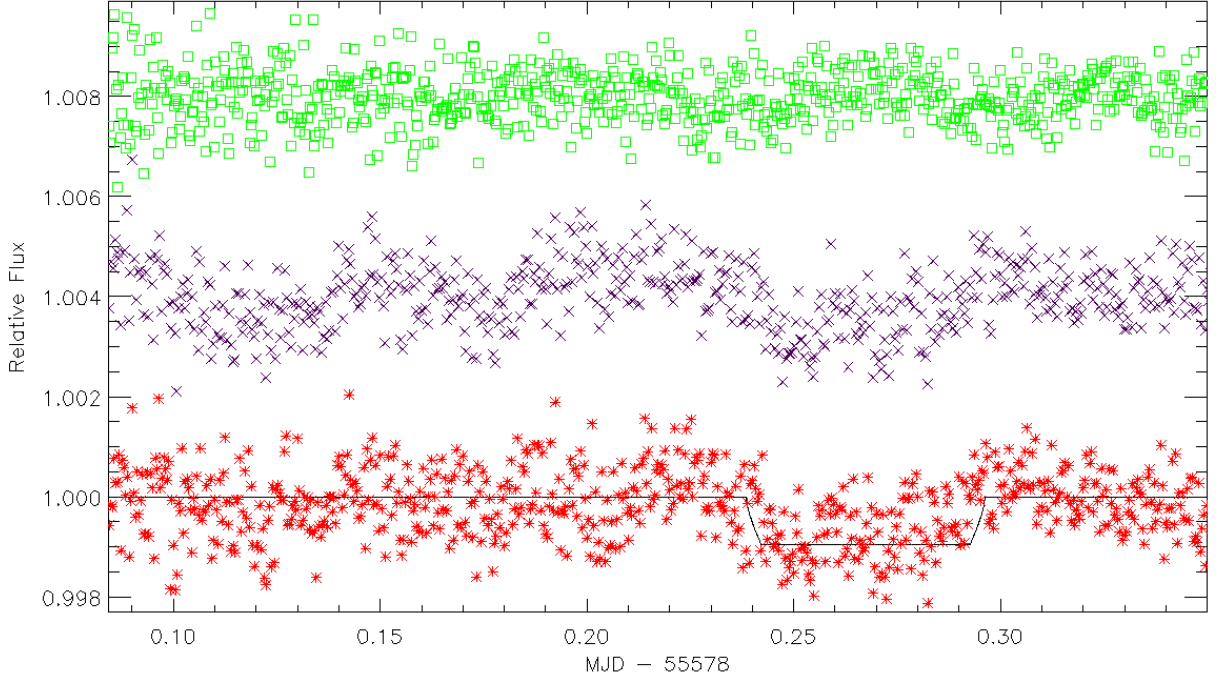


Fig. 5.— Target lightcurve pre- and post-decorrelation, normalised using a second order polynomial. The uncorrected z' -band is shown in black (central), the z' -band data after decorrelation and systematic analysis is shown in red (lower), and the green (top) points show the g' -band data with no feature at the time of secondary eclipse (as expected). The solid black line is our best-fit model of the secondary eclipse to the data.

and duration as the secondary eclipse. However, once we apply our decorrelation to this, this feature disappears, and more importantly, the feature at 0.23 to 0.3MJD (the approximate predicted ingress and egress times for the secondary eclipse) does not change. In addition to this, our analysis of the systematics on each of the comparison objects shows little variation once we apply our technique of ‘weighted comparison contribution’, indicating that whatever systematics remain are a feature of the target. During our decorrelation, the majority of features in the out-of-eclipse portion of the lightcurve were removed. After detrending, the secondary eclipse still remains at the same epoch, and appears to remain at a constant depth throughout the decorrelation and systematic removal process. As can be seen from figure 5, a number of the features present pre-ingress appear to be reduced once our sky correlation correction is applied. However, the secondary eclipse feature from ~ 0.23 -0.30MJD remains and is robust against both the systematic analysis and sky decorrelation; an indication that the feature which occurs at the predicted secondary eclipse ingress and egress times is a feature inherent to the target for this data, and not due to systematics of the comparison

objects or correlations with the sky background. The systematic analysis and decorrelation method was also applied to the g' -band, and the resulting lightcurve is also shown in figure 5 (top data points). As with the z' -band, the strongest correlation for the g' -band was with sky brightness (see appendix). We used the same method to remove this trend for both bands. The sky background correlation was much more apparent in the g' -band, and once this was removed, the remaining correlations with position, altitude etc. were significantly reduced, indicating the amount of influence the sky background has on the data set. As can be seen from figure 5, the feature which appears at the correct ingress time for the secondary eclipse in the z' -band does not appear in the g' -band, indicating the feature is unique to the z' -band. This is further evidence of the detection of the secondary eclipse, as the eclipse should be too faint to detect in the g' -band, consistent with our results. When we apply a fit to the g' -band data using the same system parameters as with the z' -band lightcurve, the routines return an eclipse depth of $0.001 \pm 0.028\%$, negligible in comparison to the z' -band. From table 1, the T_0 parameter is returned to be 2455578.7676 HJD from our analysis when we allow the transit duration to vary. In comparison to the transit ephemerides provided by Hebb et al. (2010), the predicted time of mid-eclipse, assuming a circular orbit is given to be 255578.76962 HJD. The shorter transit duration we obtain could be explained by the decrease in flux post-egress, possibly due to the observations transiting the meridian just after egress. This T_0 value corresponds to a phase of 0.490 ± 0.0047 , consistent with the results of Gibson et al. (2010) indicating that WASP-19b is in a circular orbit. We note here that while our formal statistical error from our MCMC fit is 0.0047, due to the noise present in the lightcurve as well as any systematics which remain unaccounted for, this error is likely to be higher. Since this is based on a single night's data, follow-up observations will undoubtedly further constrain the time of mid-eclipse, even observations made post-ingress will be helpful in constraining this parameter in addition to the eclipse times. When we take into account the error on the T_0 value, our transit duration agrees to the predicted value to $\sim 1.5\sigma$, a result which again can be improved upon with additional observations.

The near-infrared provides an important window for constraining the atmospheric pressure-temperature profile at depth. Atmospheric models generally indicate that the main opacity source is due to water vapour which is particularly prominent in the mid-infrared. However, in the near-infrared it has been proposed (e.g. Fortney et al. 2008, Burrows et al. 2008) that an opacity window appears which allows the atmosphere to be probed more deeply to gas lying at higher pressure. For exoplanets with temperature inversions in their atmospheres, the near-infrared emission should appear weak compared to redder observations since such planets will feature a relatively cooler atmosphere at depth compared to the hotter upper atmosphere. For planets with no temperature inversion, the gas at depth is also hot, resulting in a much reduced contrast in emission properties as one scans across multiple wave-

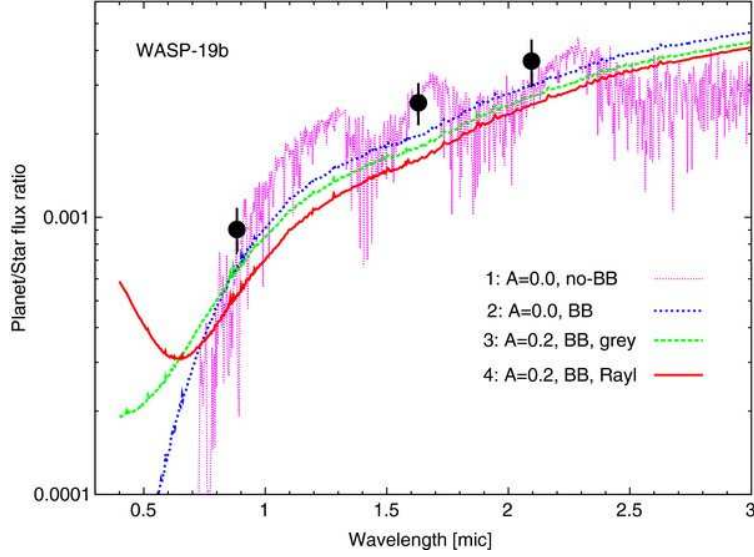


Fig. 6.— Various atmospheric models of the planet WASP-19b (from Budaj, 2011). Model 1 (dashed purple line) is the non-blackbody model based on non-irradiated atmospheres. Model 2 (dashed blue line) is a blackbody model with zero albedo. Model 3 (dashed green line) is a grey albedo model with $A_B = 0.2$. Model 4 (solid red line) is a non-grey albedo model with Rayleigh scattering and the same Bond albedo ($A_B = 0.2$). The right-hand and central black points are the K - and H -band measurements from Gibson et al. (2010) and Anderson et al. (2010) respectively. The left-hand point indicates the depth of the secondary eclipse signature from our ULTRACAM + NTT z' -band observations.

lengths. Thus, z' -band observations may provide constraints on the pressure-temperature gradient in the atmosphere, as well as an insight into the opacity mechanisms in operation (e.g. Croll et al. 2008). An eclipse depth of $0.088 \pm 0.018\%$ allows us to begin to put some constraints on the atmospheric models of the planet when combining our detection with previous secondary eclipse observations of WASP-19b (Anderson et al. 2010, Gibson et al. 2010). Figure 6 shows a modified diagram from Budaj (2011) which overplots the previously obtained H - and K -band measurements onto various atmospheric models of WASP-19b. We have also included our estimated z' -band eclipse depth in this diagram. Our secondary eclipse observation lies somewhat above the simple black-body approximation, the closest model being the $A_B=0.0$ (Bond albedo - a measure of how much energy is reflected and how much is turned into heat), non-black body model, in agreement with the previous H - and K -band measurements. Our data probes a distinctly different regime as far as the planetary atmospheric characteristics are concerned (note the logarithmic scale on the y-axis).

6. Summary

We present a detection of the secondary eclipse of the extrasolar planet WASP-19b in the Sloan z' band using the ULTRACAM CCD camera on the NTT telescope. After fitting the transit parameters, we determine a decrease in flux due to the planet passing behind the star to be $0.088 \pm 0.018\%$. Analysis of the dominant systematic effects in our data give us confidence that the feature which occurs at the predicted eclipse times is a real feature of the target. However, given the limitations of ground-based observations, especially at optical wavelengths, further observations at similar wavelengths will be of great benefit in further constraining the precise eclipse depth and T_0 for WASP-19b. In addition to this, the near-infrared remains a region over which we have yet to fully explore in regard to atmospheric characterisation, and observations such as these will allow for the atmosphere at depth to be probed for hot-Jupiters.

We have demonstrated in this paper that meaningful results for ground-based secondary eclipse detections can be achieved provided that sufficient care and attention is given to ruling out systematic variations and correlations between the flux from the target, and other observable/physical parameters.

Acknowledgements –

JB is funded by the Northern Ireland Department of Employment and learning, and in addition would like to acknowledge the support of the RMBC Queen Elizabeth Foundation. SPL acknowledges the support of an RCUK fellowship. CAW, VSD, TRM, SPL and ULTRACAM are supported by STFC. We would also like to thank the referee for providing comments and suggestions which helped improve the clarity and conciseness of the paper.

Facilities: NTT (ULTRACAM)

REFERENCES

- Alonso, R., Deeg, H. J., Kabath, P. & Rabus, M. 2010, AJ, 139, 1481
- Anderson, D. R., Gillion, M., Maxted, P. F. L. et al. 2010, A&A, 513, L3
- Budaj, J. 2011, AJ, 141, 59
- Burrows, A., Hubeny, I. & Sudarsky, D. 2005, ApJ, 625, L135
- Burrows, A., Hubeny, I. & Sudarsky, D. 2005, ApJ, 650, 1140

- Burrows, A., Ibgui, L. & Hubeny, I. 2008, *ApJ*, 682, 1277
- Collier-Cameron, A., Wilson, D. M., West, R. G. et al. 2007, *MNRAS*, 380, 1230
- Croll, B., Jayawardhana, R., Fortney, J. J., Lafrenière, D. & Albert, L. 2008, *ApJ*, 718, 920
- Deming, D., Knutson, H. A., Agol, E., Desert, J. M., Burrows, A., Fortney, J. J. et al. 2010, *ApJ*, 726, 95
- de Mooj, E. J. W. & Snellen, I. A. G. 2009, *A&A*, 493, L31
- Dhillon, V. S., Marsh, T. R., Stevenson, M. J. et al. 2007, *MNRAS*, 378, 825
- Fortney, J. J., Lodders, K., Marley, M. S. & Freedman, R. S. 2008, *AJ*, 678, 1419
- Gibson, N., Aigrain, S., Pollacco, D. et al. 2010, *MNRAS*, 404, L114
- Hebb, L., Collier-Cameron, A., Triaud, A. H. M. J. et al. 2010, *ApJ*, 708, 224
- Hellier, C., Anderson, D. R., Collier-Cameron, A. et al. 2011, *ApJ*, 730, L31
- Knutson, H. A., Charbonneau, D., Allen, L. E. et al. 2007, *Nature*, 447, 183
- Laughlin, G., Deming, D., Langton, J. et al. 2009, *Nature*, 457, 562
- Leconte, J., Lai, D. & Chabrier, G. *A&A*, 528, A41
- López-Morales, M., Coughlin, J. L., Sing, D. K. et al. 2010, *ApJ*, 716, L30
- Mandel, K. & Agol, E. 2002, *ApJ*, 580, L171
- Sing, D. K. & López-Morales, M. 2009, *A&A*, 493, L31
- Southworth, J., Hinse, T. C., Jørgensen, U. G., Dominik, M., Ricci, D., Burgdorf, M. J. et al. 2009, *MNRAS*, 396, 1023
- Zhao, M., Monnier, J. D., Swain, M., Barman, T. & Hinkley, S. 2011, *ApJ*, 748, L8

7. Appendix

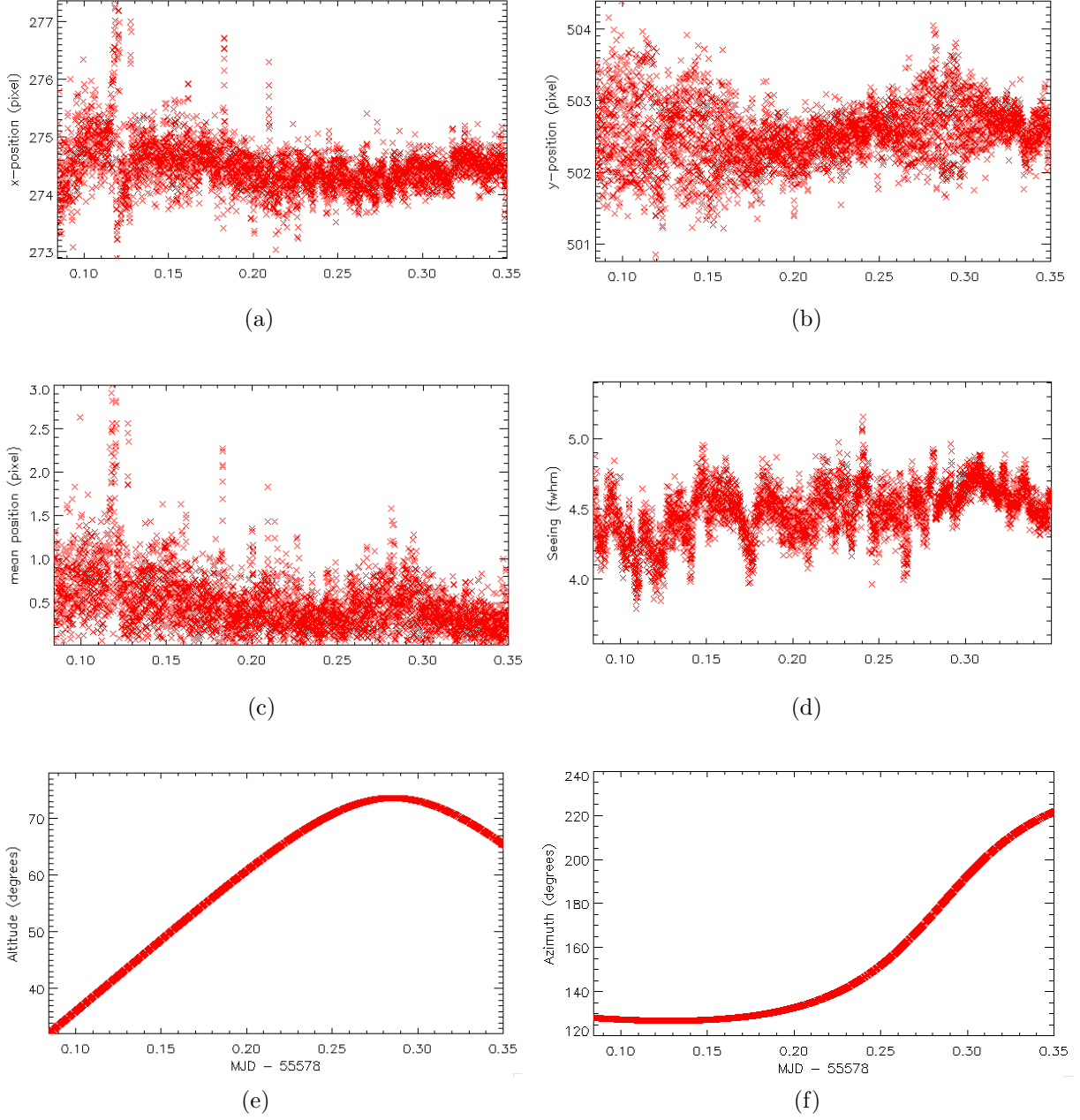


Fig. 7.— z' -band time-series of (a) x position, (b) y position, (c) mean position, (d) seeing, (e) altitude (airmass), (f) azimuth over the course of the observations.

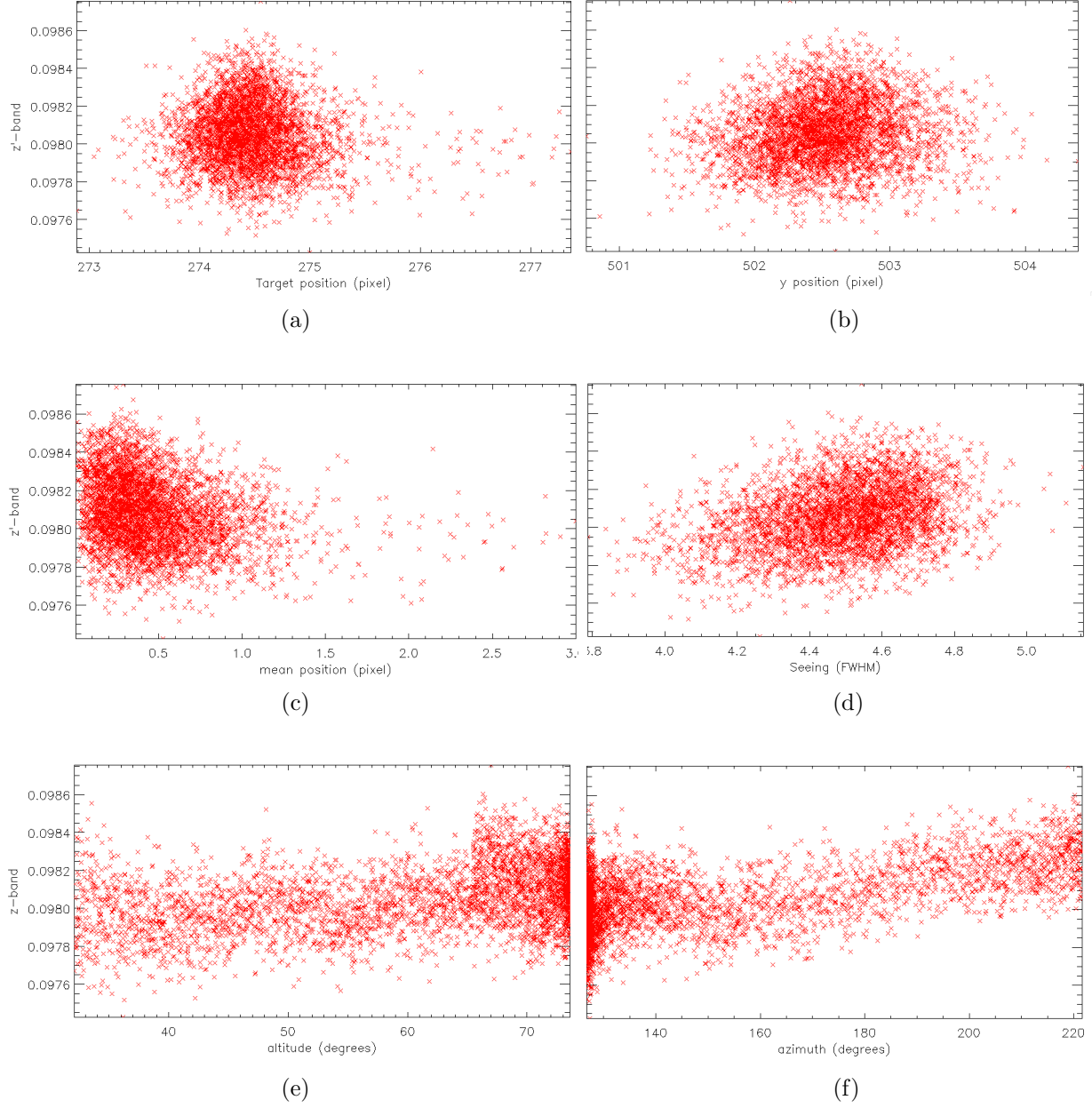


Fig. 8.— z' -band versus (a) x position. (b) y position. (c) mean position. (d) seeing. (e) altitude (airmass). (f) azimuth. Note that the target position on the chip only exhibits typically sub-pixel motion.

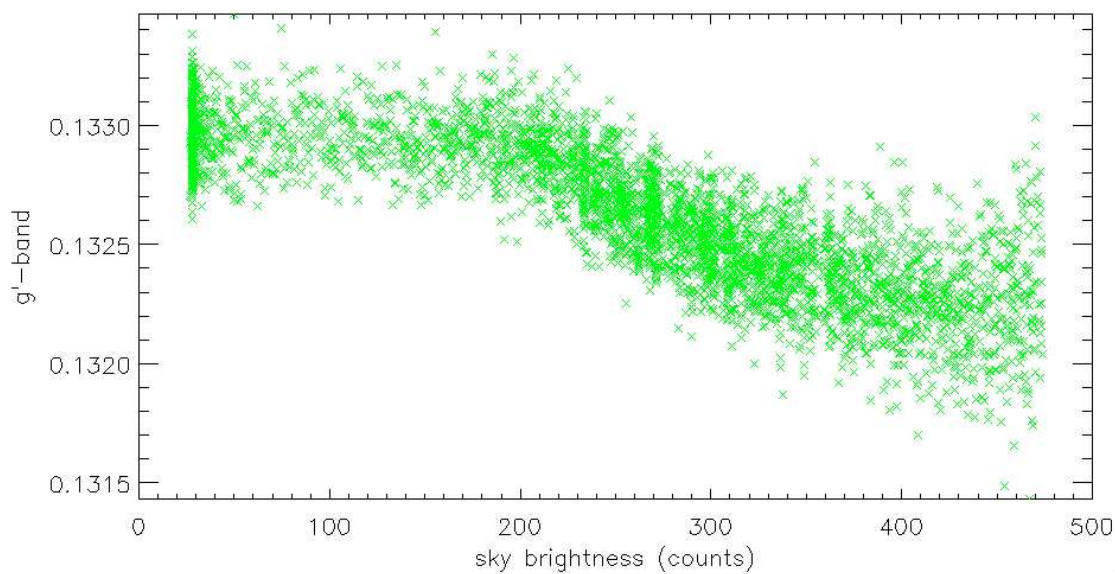


Fig. 9.— g' -band vs sky. The correlation here follows the same 2-component trend as the z' -band vs. sky background, but since the sky background is brighter relative to the target in the g' -band, this is unsurprising. Again, as with the z' -band data, a number of aperture sizes were trialled in order to assure no flux from the target was leaking into the sky aperture.

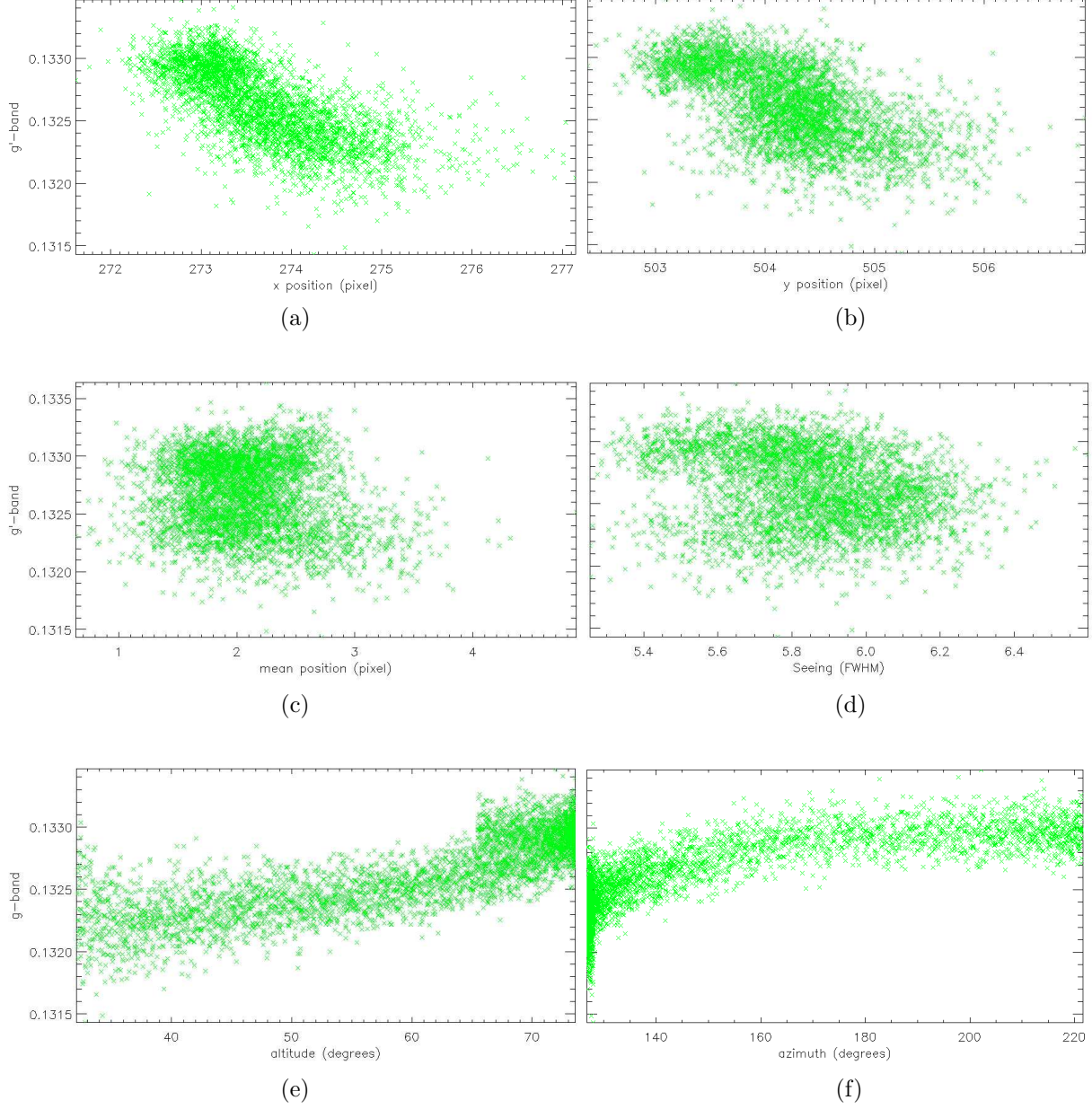


Fig. 10.— g' -band versus (a) x position. (b) y position. (c) mean position. (d) seeing. (e) altitude (airmass). (f) azimuth. Note that once the sky background (figure 9) is removed, these correlations are significantly reduced, indicating sky background is the dominant source of correlations for the data set.